Reducing the Number of Measurement Nodes in RF Imaging using Antenna Pattern Diversity with an Extended Rytov Approximation

Dingfei Ma, *Graduate Student Member, IEEE*, Amartansh Dubey, *Member, IEEE*, Zihao Xu, *Graduate Student Member, IEEE*, Shanpu Shen, *Senior Member, IEEE*, Qingfeng Zhang, *Senior Member, IEEE*, Ross Murch, *Fellow, IEEE*

***Abstract*—RF imaging that leverages existing wireless communication infrastructure, such as radio tomographic imaging (RTI) and joint communication and sensing (JCAS) is becoming increasingly important. A challenge of RF imaging is that it requires large measurement datasets containing independent measurements. In this paper we investigate a method to reduce the number of measurement nodes in RF imaging so that it is more suitable for integration with wireless communication. The approach is to exploit antenna pattern diversity so that each node can collect multiple independent measurements from the same measurement location, thereby decreasing the number of measurement nodes required. Furthermore, we formulate pattern diversity for RF imaging using the recently developed extended Rytov Approximation (xRA) which has been demonstrated to provide remarkable RF reconstruction accuracy. The advantage of utilizing xRA is that it allows us to utilize the metric of sensing capacity to straightforwardly quantify the potential of various pattern diversity configurations. Using the sensing capacity metric we are able to identify configurations where the number of measurement nodes can be reduced by at least a factor of two. Simulation results are provided to verify the RF imaging approach with reduced measurement nodes, which demonstrates the potential of using pattern diversity.**

***Index Terms*—Inverse scattering, RF imaging, Pattern diversity, Radio Tomographic Imaging (RTI), Rytov approximation, extended Rytov approximation.**

I. Introduction

Radio frequency (RF) and microwave imaging [1], [2] have a wide range of applications including indoor RF imaging [3], [4], [5], [6], non-destructive testing [7], biomedical diagnosis [8], [9], [10], [11], through-the-wall imaging, rescue operations, security-screening and more generally inverse scattering [12], [13], [14], [15]. Of these applications, those that can utilize existing wireless communication infrastructure have attracted significant recent attention and include techniques such as radio tomographic imaging (RTI) [16], [17], [18], [19], [20] and joint communication and sensing (JCAS). These RF imaging techniques can leverage existing wireless communication platforms such as WiFi for convenient deployment. However RF imaging typically requires large measurement data sets containing independent measurements and these are obtained in a variety of ways. For indoor RF imaging using RTI, 20-40 WiFi nodes are usually utilized around the imaging region [5], [6]. This implies that a conventional WiFi network must be supplemented with additional WiFi nodes specifically dedicated to the imaging application. If the requirement for the number of measurement nodes in RF imaging could be reduced then the deployment difficulties of these imaging systems could also be reduced.

Frequency diversity has been exploited as one way to increase the number of independent measurements that can be obtained from a measurement node [21], [22], [23]. These techniques typically use dispersive antenna structures to achieve frequency diversity [21], [22], [23], [24], [25]. As the frequency sweeps through its given frequency range, the antenna pattern scans through an angular range or changes significantly providing the necessary diversity. A disadvantage of this approach is the wide frequency bandwidth that is required making it unsuitable for existing wireless communication applications.

A more straightforward approach to achieve the required measurement diversity is to utilize antenna pattern diversity directly. In recent years, a large number of antenna designs that can provide digitally controlled patterns have been proposed. In [26], pattern diversity is achieved by switching parasitic elements. Other ways to achieve controlled patterns is to use pixel antennas [27]. The antenna can generate different radiation patterns by controlling switches or PIN diodes connected between pixels and a variety of designs have been proposed [27], [28], [29]. In applying these antennas to RF imaging, the exact type of pattern is not critical as long as it is sufficiently different to provide independent measurements. If enough spatial information can be captured through the various radiation patterns then the number of measurement nodes can be reduced.

There have also been developments in reconstruction techniques for RF imaging. Over the last decade, RTI has been developed and now provides a straightforward imaging approach to estimate shape, size and location of the target

This work is supported by the Hong Kong grants council CRF grant C6012-20G and in part by GuangDong Basic and Applied Basic Research Foundation (2021B1515120029). (Corresponding author: Amartansh Dubey; Qingfeng Zhang).

D. Ma, A. Dubey, Z. Xu and R. Murch are with Department of Electronic and Computer Engineering at the University of Hong Kong Science and Technology, Hong Kong.

S. Shen is with the Department of Electrical Engineering and Electronics, University of Liverpool, Liverpool L69 3GJ, U.K. (email: Shanpu.Shen@liverpool.ac.uk).

Q. Zhang is with the Shenzhen Key Laboratory of Electromagnetics and also with the Department of Electronics and Electrical Engineering, Southern University of Science and Technology, Shenzhen, Guangdong, 518055, China. (email: zhang.qf@sustech.edu.cn).

objects. More formal inverse scattering approaches have also been investigated for use with RF imaging. Non-linear state-of-the-art techniques have been developed to overcome the limits on reconstruction quality including subspace optimization (SOM) and contrast source inversion (CSI) [13], [30]. However they require higher computational loads and are sensitive to the experimental errors and noise due to their non-linear formulation while only moderately extending the range of permittivity and size that can be handled. This prevents their application to a large domain of interest (DOI) such as indoor imaging [31]. While linear techniques are robust to such noise and errors, the common linearized methods of the Born approximation (BA) and Rytov approximation (RA) are limited to reconstructing relative permittivity close to unity [4], [31]. Iterative linear methods have also been proposed for strong scattering conditions including the distorted wave Born iterative method (DBIM) and the distorted wave Rytov iterative method (DRIM) [32], [33], [34], [35]. Recent results based on a linear formulation denoted as the extended Rytov approximation (xRA) [3], [14], [36], [37] has shown that significant further improvements are possible in the validity range of RA including accurate reconstruction of objects up to relative permittivities of $\epsilon = 15 + j1.5$ for object sizes greater than 30 wavelengths. Even at higher relative permittivities of up to $\epsilon = 77 + j7$ object shape reconstruction remains accurate in xRA, however the reconstruction amplitude is less accurate [3], [36]. In short, xRA provides a straightforward linear reconstruction technique that performs at least as well as state-of-the-art non-linear techniques and can be applied to RF imaging conveniently.

In this paper, we develop and investigate the use of pattern diversity for reducing the number of required measurement nodes in utilizing xRA for RF imaging. Specific contributions of this work include formulating pattern diversity for use with xRA. More importantly we apply sensing capacity to xRA in order to provide guidelines for the pattern configurations to reduce the number of measurement nodes by at least a factor of two. Neither pattern diversity or the use of sensing capacity have been investigated in our previous work [3], [6]. The novelty of our work lies in investigating the antenna pattern diversity technique and its evaluation using sensing capacity to reduce the number of measurement nodes in xRA based RF imaging applications. This can potentially make xRA more suitable for practical settings and also allow its integration into wireless communications. Simulation results of RF imaging utilizing pattern diversity based on full three-dimensional (3D) electromagnetic simulations are also provided to verify the proposed techniques. The results obtained show that the number of measurement nodes can be at least halved to greatly reduce the number of required transceivers in the imaging system.

The remainder of this paper is organized as follows. In section II, we provide the forward scattering model for the proposed antenna pattern diversity RF imaging configuration. The formulation of the corresponding inverse scattering problem using xRA with pattern diversity is described in section III. In section IV, the concept of sensing capacity is introduced to provide straightforward estimates of the reconstruction quality that can be obtained with reduced numbers of measurement nodes and pattern diversity. In section V, simulation results are obtained using a full 3D electromagnetic simulator and these demonstrate the potential of using pattern diversity. Discussions are provided in section VI, and finally conclusions are provided in section VII.

Notation: Lower case boldface letters $\mathbf{x}$ refer to position vectors. Single overline upper and lower case letters $\left(\overline{X}\right)$ or $\left(\overline{x}\right)$ denote vectors and double overline upper and lower case letters $\left(\overline{\overline{X}}\right)$ or $\left(\overline{\overline{x}}\right)$ denote matrices. Italic letters represent scalar parameters. $(\cdot)^T$ and $(\cdot)^{-1}$ represent transpose and inverse operation, respectively. $\mathbb{C}$ denotes complex set. $\omega = 2\pi f$ is the angular frequency and wavenumber is defined as $k_0 = 2\pi/\lambda = \omega_0\sqrt{\epsilon_0\mu_0}$, where λ is wavelength and ϵ_0 and μ_0 are free space permittivity and permeability respectively.

II. Problem Formulation

A. Configuration

To provide a practical context for RF imaging, we consider a typical indoor environment as shown in Fig. 1. However any suitable RF imaging application such as non-destructive testing is equally viable. The DOI considered is a two-dimensional (2D) planar cross-section through the floor at height L_h. The 2D cross-section is also drawn in abstract form in Fig. 1 where the scatterers refer to the 2D cross-section of objects in the DOI. The scatterers are assumed non-magnetic with complex permittivity $\epsilon(\mathbf{r}) = \epsilon_R(\mathbf{r}) + j\epsilon_I(\mathbf{r})$ that are taken as low-loss where $\epsilon_I(\mathbf{r}) \ll \epsilon_R(\mathbf{r})$. Most objects around us exhibit low loss behavior at radio and microwave frequencies [3]. The background medium is homogeneous with $\epsilon_0(\mathbf{r}) = 1$, and consists of air for the indoor environment. In our RF imaging system the DOI is restricted to the area $L_x \times L_y$, and is discretized into $N_x \times N_y$ pixels where $N_x = L_x/\Delta x$, $N_y = L_y/\Delta y$ are the number of spatial pixels in the $x-y$ plane and have area $\Delta\Omega = \Delta x\Delta y$. The total number of spatial pixels is denoted as $N = N_x \times N_y$ within the DOI and a particular pixel is identified by the integer n with $n \in (1, N)$.

In Fig. 1, $M = 20$ transceiver measurement nodes (such as WiFi access points) are shown evenly distributed on the rectangular measurement boundary $\mathcal{B}$ around the DOI. The location of the mth transmitting antenna is denoted by $\mathbf{r}_m$ and the location of the m' receiving antenna is denoted by $\mathbf{r}_{m'}$ where $\mathbf{r}_m, \mathbf{r}_{m'} \in \mathcal{B}$. Note that, the subscripts m and m' refer to the mth transmitting and m'th receiving antenna respectively in the remainder of this manuscript. In general the $m = m'$ transmit and receiver pair will be co-located and therefore a constraint will be that they cannot receive and transmit simultaneously. $\mathbf{r}_n \in \mathcal{D}$ refers to an arbitrary point in the DOI and distances $\mathbf{r}_{m,n}$ and $\mathbf{r}_{n,m'}$ are the distances between the point $\mathbf{r}_n$ and the transmitting antenna m and receiving antenna m' respectively. Angle $\phi_{m,n}$ denotes the angles at the mth transmitting antenna to the DOI point $\mathbf{r}_n$, angle $\phi_{m',n}$ refers to the angle between the m'th receiving antenna and $\mathbf{r}_n$.

In the RF imaging system, vertically polarized antennas in a transverse-magnetic (TM) formulation are used for the nodes, where the vertical direction is defined as being along

the z-axis as shown. To constrain the imaging problem to 2D cross-sections the antennas have directive patterns that radiate primarily into the $x-y$ plane and this follows the approach in previous work [5], [6], [16], [17], [18], [19], [20].

In conventional indoor RF imaging approaches such as RTI [16], [17], [18], [19], [20] and recent Rytov [5], [6] based approaches the patterns of all the antennas are fixed. In addition, the transmitter and receiver at each node are often collocated and share the same antenna such as in WiFi. Therefore for transmission at the mth node, measurements are collected from the other $M-1$ nodes ($m' \neq m$ with $m \in (1, M)$). In total we can therefore obtain measurements from $M(M-1)$ possible links. However, because all the nodes typically have identical antennas, and the transmitter and receiver share the same antenna, the node links will be reciprocal and the independent measurements L are half and given by [6]

$$L = M\left(M-1\right)/2. \tag{1}$$

To gather sufficient measurement data, the number of transmitter and receiver nodes therefore needs to be large and for areas approximately $5 \times 5\, m^2$, the number of nodes should be large and at least $M > 20$ [5], [6], [17].

For RF imaging to be more widely applicable and leverage existing wireless architecture it is necessary to try and reduce the number of measurement nodes. Inspired by recent results on pattern diverse microwave imaging systems, in this work we incorporate pattern diversity at the nodes [23]. That is when a node is transmitting it may select one of P antenna patterns at the transmitter and one of Q patterns at the receiver. If the P patterns are all different from the Q receive patterns, the total number of unique measurement links is $L = M\left(M-1\right)PQ$. A special case is when the transmitter and receiver share the antennas so that $P = Q$ and the transmit and receive patterns are all identical. For this special case the number of unique links will be $L = M\left(M-1\right)PQ/2$ since the links will again be reciprocal.

The general expression for the number of independent links when $P \geq Q$ in which Q receive patterns out of the P transmit patterns are identical can be written as

$$L = M(M-1)Q(P-Q/2). \tag{2}$$

This is because $M(M-1)QQ/2$ links exhibit reciprocity since they share the same receive and transmit antennas. The remaining $M(M-1)(P-Q)Q$ links will not exhibit reciprocity providing $L = M(M-1)Q(P-Q/2)$ unique links (2). This expression can be easily modified for $Q > P$ by interchanging P with Q. In this general configuration, by comparing (2) with (1), utilizing pattern diversity provides $2Q(P-Q/2)$ more links than without pattern diversity.

B. Formulation

To formulate the RF imaging system consider the incident field, $E^{\mathrm{i}}_{m,p}\left(\mathbf{r}_n\right)$, from the mth transmitting antenna at position $\mathbf{r}_n$ using its pth pattern. The scattered and total electric fields resulting from this incident field are defined as

$$E^{\mathrm{t}}_{m,p}\left(\mathbf{r}_n\right) = E^{\mathrm{i}}_{m,p}\left(\mathbf{r}_n\right) + E^{\mathrm{s}}_{m,p}\left(\mathbf{r}_n\right), \tag{3}$$

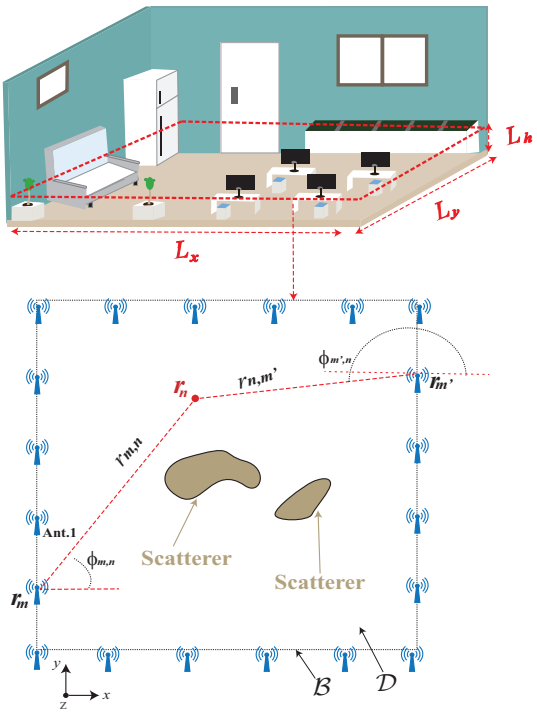

Fig. 1. RF imaging in the context of an indoor environment. The DOI considered is a 2D planar cross-section through the floor at height L_h. The 2D cross-section is also illustrated in abstract form where the scatterers refer to the 2D cross-section of objects in the DOI. The DOI has $M = 20$ measurement nodes at its boundary $\mathcal{B}$ and dimensions $L_x \times L_y$ at cross-sectional height L_h. Further details for the notation is provided in the associated text.

in which $E^{\mathrm{t}}_{m,p}\left(\mathbf{r}_n\right)$ and $E^{\mathrm{s}}_{m,p}\left(\mathbf{r}_n\right)$ refer to the total and scattered electric fields produced by the mth transmitting antenna under pth pattern at position $\mathbf{r}_n$ respectively. In discretized form, the forward problem for obtaining the scattered electric field on the boundary of the DOI can be written utilizing the Lippman–Schwinger integral equation as [13], [38]

$$E^{\mathrm{s}}_{m,p}\left(\mathbf{r}_{m'}\right) = -j\omega\mu_0 \sum_{\forall n | \mathbf{r}_n \in D} g\left(\mathbf{r}_{m'}, \mathbf{r}_n\right) E^{\mathrm{t}}_{m,p}\left(\mathbf{r}_n\right) \cdot \chi_c\left(\mathbf{r}_n\right) \Delta\Omega\,, \tag{4}$$

where $\chi_c\left(\mathbf{r}_n\right) = \epsilon\left(\mathbf{r}_n\right) - \epsilon_0$ and $g\left(\mathbf{r}_{m'}, \mathbf{r}_n\right)$ denotes Green's function

$$g\left(\mathbf{r}_{m'}, \mathbf{r}_n\right) = \frac{-\eta\pi a}{2} J_1\left(k_0 a\right) H_0^{(1)}\left(k_0 \mid \mathbf{r}_{m'} - \mathbf{r}_n \mid\right), \tag{5}$$

where $a = \sqrt{\Delta\Omega/\pi}$ is the radius of the circle of the same area of the square cell, $k_0 = 2\pi/\lambda$ is the wavenumber and $\Delta\Omega$ is the area of each square cell [6], [31]. $J_1\left(\cdot\right)$ is the Bessel function of the first kind, order 1 and $H_0^{(1)}\left(\cdot\right)$ is the Hankel function of the first kind, order 0. $\eta = 377$ ohm is the impedance of free space.

In practice, the scattered field $E^{\mathrm{s}}_{m,p}\left(\mathbf{r}_{m'}\right)$ is sensed by a receiving antenna and converted to a received voltage. To incorporate this into (4) we follow previous approaches [1], [6], [39] where the Green's function in (4) is replaced by the electric field radiated by the receiving antenna in free-space

when it is configured in transmitting mode with unit excitation. Using this approach we rewrite (4) as

$$V_{m,p}^{m',q} = \frac{-j\omega\mu_0}{a} \sum E^{\mathrm{i}}_{m',q}(\mathbf{r}_n)\, E^{\mathrm{t}}_{m,p}(\mathbf{r}_n)\, \chi_c(\mathbf{r}_n)\, \Delta\Omega\,, \quad (6)$$

where $E^{\mathrm{i}}_{m',q}(\mathbf{r}_n)$ is the field radiated from the receiver when it is configured as a transmitter with a unit excitation and positioned at m' with pattern q, [1], [39]. The voltage $V_{m,p}^{m',q}$ is the received voltage at node m' with pattern q due to a scattered field arising from the incident field at the mth node using pattern p. The constant a is for normalization and can be found from [1], [6], [39].

The goal of the direct or forward problem can then be stated as estimating the voltage $V_{m,p}^{m',q}$ at the receivers given the permittivity profile $\epsilon(\mathbf{r}_n)$ and known incident fields. The goal of the inverse problem or RF imaging, on the other hand, is to estimate $\chi_c(\mathbf{r}_n)$ given only voltage measurements $V_{m,p}^{m',q}$ at the receivers. The inverse problem is considered more difficult than the direct problem because there are usually fewer measurements than unknowns and both $\chi_c(\mathbf{r}_n)$, $E^{\mathrm{t}}_{m,p}(\mathbf{r}_n)$ are unknown inside the DOI. For these reasons the inverse problem is ill-posed and non-linear.

III. Inverse Scattering Problem

A. Extended Rytov approximation

Recent new results for an enhanced linear approximation, xRA, [3], [36] have shown that excellent reconstruction accuracy is possible without intricate non-linear processing. Compared with RA, xRA enhances the validity range by utilizing a high-frequency approximation for waves passing through lossy scatterers.

To obtain the xRA formulation with pattern diversity we follow RA, and write the total field $E^{\mathrm{t}}_{m,p}(\mathbf{r}_n)$ as [40], [41]

$$E^{\mathrm{t}}_{m,p}(\mathbf{r}_n) = E^{\mathrm{i}}_{m,p}(\mathbf{r}_n)\, e^{\phi^{\mathrm{s}}_{m,p}(\mathbf{r}_n)}, \quad (7)$$

where $\phi^{\mathrm{s}}_{m,p}(\mathbf{r}_n)$ can be thought of as complex scattered wavefronts. Then, utilizing the Rytov transform

$$\tilde{E}_{m,p}(\mathbf{r}_n) = E^{\mathrm{i}}_{m,p}(\mathbf{r}_n) \ln\left(\frac{E^{\mathrm{t}}_{m,p}(\mathbf{r}_n)}{E^{\mathrm{i}}_{m,p}(\mathbf{r}_n)}\right), \quad (8)$$

we find that $\tilde{E}_{m,p}(\mathbf{r}_n)$ satisfies

$$\nabla^2\tilde{E}_{m,p}(\mathbf{r}_n) + k^2\tilde{E}_{m,p}(\mathbf{r}_n) = -k_0^2\chi_{RT}(\mathbf{r}_n)\, E^{\mathrm{i}}_{m,p}(\mathbf{r}_n)\,, \quad (9)$$

where

$$\chi_{\mathrm{RT}}(\mathbf{r}_n) = \nu^2(\mathbf{r}_n) - 1 - \nabla\phi^{\mathrm{s}}_{m,p}(\mathbf{r}_n)\cdot\nabla\phi^{\mathrm{s}}_{m,p}(\mathbf{r}_n)\,, \quad (10)$$

where $\nu(\mathbf{r})$ refers to the refractive index and is related to $\epsilon(\mathbf{r})$ by $\nu^2(\mathbf{r}) = \epsilon(\mathbf{r})$. Using (4) we can write (9) in discrete form as

$$\tilde{E}_{m,p}(\mathbf{r}_{m'}) = -j\omega\mu_0 \sum_{\forall n|\mathbf{r}_n\in D} g(\mathbf{r}_{m'},\mathbf{r}_n)\, E^{\mathrm{i}}_{m,p}(\mathbf{r}_n) \cdot \chi_{\mathrm{RT}}(\mathbf{r}_n)\,\Delta\Omega\,. \quad (11)$$

We refer to $\chi_{\mathrm{RT}}(\mathbf{r}_n)$ as the contrast function when using the Rytov transform. Finding the term $\nabla\phi^{\mathrm{s}}_{m,p}(\mathbf{r}_n)\cdot\nabla\phi^{\mathrm{s}}_{m,p}(\mathbf{r}_n)$ in $\chi_{\mathrm{RT}}(\mathbf{r}_n)$ (10) is difficult because the wavefronts $\phi^{\mathrm{s}}_{m,p}(\mathbf{r}_n)$ depend on the total field which remains unknown. To handle this issue conventional RA ignores the term $\nabla\phi^{\mathrm{s}}_{m,p}(\mathbf{r}_n)\cdot\nabla\phi^{\mathrm{s}}_{m,p}(\mathbf{r}_n)$ under the assumption of weak scattering, which results in the contrast function

$$\chi_{RA}(\mathbf{r}_n) = \nu^2(\mathbf{r}_n) - 1 = \epsilon(\mathbf{r}_n) - 1. \quad (12)$$

This makes the solution for the object permittivity straightforward as there are then no other unknowns on the right hand side of (9) and a linear equation can be formed. However the range of validity on permittivity to achieve accurate reconstructions is limited since ignoring $\nabla\phi^{\mathrm{s}}_{m,p}(\mathbf{r}_n)\cdot\nabla\phi^{\mathrm{s}}_{m,p}(\mathbf{r}_n)$ is only valid under weak scattering conditions. For large scatterers with high permittivity variations, the term $\nabla\phi^{\mathrm{s}}_{m,p}(\mathbf{r}_n)\cdot\nabla\phi^{\mathrm{s}}_{m,p}(\mathbf{r}_n)$ may be significant and cannot be neglected. To enhance RA, an approximation to $\nabla\phi^{\mathrm{s}}_{m,p}(\mathbf{r})\cdot\nabla\phi^{\mathrm{s}}_{m,p}(\mathbf{r})$ by a high-frequency approximation for waves passing through lossy scatterers has been proposed and this has led to xRA [3], [36].

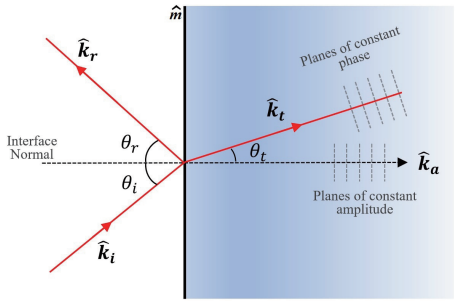

Fig. 2. Free space to lossy media interface. The homogeneous plane wave in free space becomes an inhomogeneous plane wave in the lossy media on the right hand side (with constant refractive index $\nu = \nu_R + j\nu_I$) [3], [36].

In xRA the transmitted field resulting from an incident plane wave $E^{\mathrm{i}}_{m,p}(\mathbf{r}_n) = A^{\mathrm{i}}_{m,p}(\mathbf{r}_n)\exp(jk_0\,\hat{\boldsymbol{k}}_i\cdot\mathbf{r}_n)$, passing into a lossy media $\boldsymbol{\epsilon}$ half-space (see Fig. 2) is written as

$$E^{\mathrm{t}}_{m,p}(\mathbf{r}_n) = A^{t}_{m,p}(\mathbf{r}_n)\exp(jk_0\,(V_R\hat{\boldsymbol{k}}_{\boldsymbol{t}}\cdot\mathbf{r}_n + jV_I\hat{\boldsymbol{k}}_{\boldsymbol{a}}\cdot\mathbf{r}_n)), \quad (13)$$

where unit vectors $\hat{\boldsymbol{k}}_i$, $\hat{\boldsymbol{k}}_{\boldsymbol{t}}$ and $\hat{\boldsymbol{k}}_{\boldsymbol{a}}$ refer to the directions of the incident field, transmitted field and the normal to the planar interface of the half space respectively also as illustrated in Fig. 2 [3], [36]. $A^{\mathrm{i}}_{m,p}(\mathbf{r}_n)$ and $A^{t}_{m,p}(\mathbf{r}_n)$ are the magnitude of the incident and transmitted fields at position $\mathbf{r}_n$ respectively and V_R and V_I are termed as real and imaginary part of the refractive index respectively [3], [36]. Based on (13), the term $\nabla\phi^{\mathrm{s}}_{m,p}(\mathbf{r}_n)\cdot\nabla\phi^{\mathrm{s}}_{m,p}(\mathbf{r}_n)$ in $\chi_{\mathrm{RT}}(\mathbf{r}_n)$ (10) can be derived and substituted into (10) so that the contrast function for xRA becomes (see detailed derivation of xRA in [3], [36])

$$\chi_{\mathrm{xRA}}(\mathbf{r}_n) = 2\left(\sqrt{\epsilon_R(\mathbf{r}_n)}\cos\theta_s(\mathbf{r}_n) - 1\right) + \frac{j\epsilon_I(\mathbf{r}_n)\cos\theta_i(\mathbf{r}_n)}{\sqrt{\epsilon_R(\mathbf{r}_n) - \sin^2\theta_i(\mathbf{r}_n)}}. \quad (14)$$

where $\theta_i = \cos^{-1}\left(\hat{\boldsymbol{k}}_{\boldsymbol{i}}\cdot\hat{\boldsymbol{k}}_{\boldsymbol{a}}\right)$ and $\theta_s = \cos^{-1}\left(\hat{\boldsymbol{k}}_{\boldsymbol{t}}\cdot\hat{\boldsymbol{k}}_{\boldsymbol{i}}\right)$ refer to the incident and scattering angles respectively. As explained in [3], [36] the dependence of the imaginary part of the contrast $\mathrm{Im}(\chi_{\mathrm{RI}})$ on θ_i instead of θ_s is the most important aspect of (14). The incident angle θ_i is only a function of the shape

of the object. It does not change with the permittivity of the object. This implies that any distortion in the imaginary component, $\mathrm{Im}(\chi_{\mathrm{RI}})$, of the reconstruction due to the presence of the θ_i terms is independent of the objects permittivity. Therefore, if the imaginary component of the reconstruction is accurate at low permittivity, it is likely to be accurate for all permittivity levels. This is the reason the imaginary part of the contrast function $\chi_{\mathrm{xRA}}(\mathbf{r}_n)$ is the focus and in [3], [36] it is demonstrated that it can be reconstructed very accurately. The real part of $\chi_{\mathrm{xRA}}(\mathbf{r}_n)$ is reconstructed less accurately and therefore discarded.

By performing averaging over θ_i in (14), the final expression for the imaginary part of the xRA contrast function is written as [3]

$$\mathrm{Im}\left(\chi_{\mathrm{xRA}}(\mathbf{r}_n)\right) = \frac{2\epsilon_I(\mathbf{r}_n)}{\pi}\sin^{-1}\left(\frac{1}{\sqrt{\epsilon_R(\mathbf{r}_n)}}\right). \tag{15}$$

In xRA the same reconstruction procedure as RA is utilized except an additional step is required in the final processing. That is only the imaginary part of the reconstruction is utilized and equated to $\mathrm{Im}\left(\overline{\chi}_{\mathrm{xRA}}\right) = 2/\pi\epsilon_I(\mathbf{r}_n)\sin^{-1}\left(1/\sqrt{\epsilon_R(\mathbf{r}_n)}\right)$. This is very different from conventional RA where the real part is taken as a reconstruction of $\epsilon(\mathbf{r}_n)-1$. Accurate reconstructions of (15) for a wide range of materials found in the everyday environment can be obtained [3], [36]. Since the reconstruction of (15) is a function of both real and imaginary parts of the permittivity, it is shown to provide not only shape reconstruction, but it also helps to distinguish between a wide range of objects in the indoor environment based on their permittivity. For example it has been shown that xRA provides accurate reconstruction of scatterers up to relative permittivities of $15+j1.5$ for scatterer sizes greater than 30 wavelengths [3], [36] and continues to provide accurate shape reconstruction up to $70+j7$ [3], [14].

As a final step in the formulation of xRA we need to relate it to the received voltages at the receivers. To perform this in xRA the source term in (11) is replaced with $\chi_{xRA}(\mathbf{r}_n)$ to obtain

$$\tilde{V}_{m,p}^{m',q} = \frac{-j\omega\mu_0}{a}\sum E_{m',q}^{\mathrm{i}}(\mathbf{r}_n)\, E_{m,p}^{\mathrm{i}}(\mathbf{r}_n)\,\chi_{xRA}(\mathbf{r}_n)\,\Delta\Omega\,, \tag{16}$$

where

$$\tilde{V}_{m,p}^{m',q} = \mathring{V}_{m,p}^{m',q}\ln\frac{\dot{V}_{m,p}^{m',q}}{\mathring{V}_{m,p}^{m',q}}. \tag{17}$$

In (17), $\mathring{V}_{m,p}^{m',q}$ refers to the background measurement with no scatterers (received voltage due to the incident field alone) and $\dot{V}_{m,p}^{m',q}$ refers to the total received voltage due to the scattered and incident fields.

Writing (16) as a set of linear equations for all $M(M-1)Q(P-Q/2)$ measurements we obtain

$$\overline{V} = \overline{\overline{H}}\,\overline{\chi}_{\mathrm{xRA}}, \tag{18}$$

where $\overline{V} \in \mathbb{C}^{M(M-1)Q(P-Q/2)\times 1}$ refers to the received response vector consisting of $\tilde{V}_{m,p}^{m',q}$ for all M transceivers, P transmitting patterns and Q receiving patterns and it is arranged as $\overline{V} = \left[\overline{V}_1;\ldots\overline{V}_m;\ldots\overline{V}_M\right]$, with $\overline{V}_m = \left[\overline{V}_{1,m};\ldots\overline{V}_{m',m};\ldots\overline{V}_{(M-1),m};\right]$, $\overline{V}_{m',m} = \left[\overline{V}_{m',m,1};\ldots\overline{V}_{m',m,q};\ldots\overline{V}_{m',m,Q};\right]$ and $\overline{V}_{m',m,q} = \left[\tilde{V}_{m,1}^{m',q};\ldots\tilde{V}_{m,p}^{m',q};\ldots\tilde{V}_{m,P}^{m',q}\right]$. The contrast vector $\overline{\chi}_{RA} \in \mathbb{C}^{N\times 1}$ contains elements $\chi_{\mathrm{RA}}(\mathbf{r}_n)$ for $n = 1,2\ldots N$ and $\chi_{\mathrm{RA}}(\mathbf{r}_n)$ is defined in (10). $\overline{\overline{H}} \in \mathbb{C}^{M(M-1)Q(P-Q/2)\times N}$ refers to the measurement matrix and it is arranged by $\overline{\overline{H}} = \left[\overline{\overline{H}}_1;\ldots\overline{\overline{H}}_m;\ldots\overline{\overline{H}}_M\right]$, with $\overline{\overline{H}}_m = \left[\overline{\overline{H}}_{1,m};\ldots\overline{\overline{H}}_{m',m};\ldots\overline{\overline{H}}_{(M-1),m};\right]$, $\overline{\overline{H}}_{m',m} = \left[\overline{\overline{H}}_{m',m,1};\ldots\overline{\overline{H}}_{m',m,q};\ldots\overline{\overline{H}}_{m',m,Q};\right]$ and $\overline{\overline{H}}_{m',m,q} = \frac{-j\omega\mu_0}{a}\left[\overline{E}_{m',q}^{\mathrm{i}}\overline{E}_{m,1}^{\mathrm{i}}\ldots\overline{E}_{m',q}^{\mathrm{i}}\overline{E}_{m,p}^{\mathrm{i}}\ldots\overline{E}_{m',q}^{\mathrm{i}}\overline{E}_{m,P}^{\mathrm{i}}\right]^T$. The vector $\overline{E}_{m',q}^{\mathrm{i}} \in \mathbb{C}^{N\times 1}$ contains elements $E_{m,q}^{\mathrm{i}}(\mathbf{r}_n)$ for $n = 1,2\ldots N$ and is the incident electrical field vector within DOI produced by the receiving node m' at the qth pattern.

B. Reconstruction and Regularization

In order to retrieve the object from the acquired measurements in (18), we need to handle the issue that the number of independent observations $M(M-1)Q(P-Q/2)$ is generally much less than the unknowns N. Using the condition of sparsity, it is possible to utilize compressive sensing (CS) algorithms to solve this under-determined problem (18). This can be written as

$$\min_{\overline{\chi}_{\mathrm{xRA}}} \|\overline{\chi}_{\mathrm{xRA}}\|_{l_1} \ \text{ s.t. } \overline{V} = \overline{\overline{H}}\,\overline{\chi}_{\mathrm{xRA}}, \tag{19}$$

where $\|\cdot\|_{l_1}$ denotes the l_1 norm. Here we employ the two-step iterative shrinkage thresholding (TwIST) algorithm [42]. Once this is performed we take the imaginary part of the contrast function to reconstruct $\mathrm{Im}\left(\overline{\chi}_{\mathrm{xRA}}\right) = 2/\pi\epsilon_I(\mathbf{r}_n)\sin^{-1}\left(1/\sqrt{\epsilon_R(\mathbf{r}_n)}\right)$.

IV. Sensing Capacity with Pattern Diversity

A unique aspect of xRA is its wide validity range while still having a linear formulation (18). Its linear formulation allows us to directly apply the concept of sensing capacity [43], [44] to determine whether a particular antenna configuration and their patterns will perform better than other configurations. In this section we introduce sensing capacity and provide a model for the antenna patterns so that it can be applied to determine the most appropriate pattern configurations for reducing the number of measurement nodes.

A. Sensing Capacity

One method to quantitatively evaluate the imaging performance of a system (18) is by using sensing capacity [43]. Applying singular value decomposition (SVD) to measurement matrix $\overline{\overline{H}}$ we can obtain its eigenvalue distribution [45]. Using these eigenvalues sensing capacity [43] is defined as

$$C = \sum_{k=1}^{K}\log\left(1+\frac{P_k\lambda_k}{N_0}\right), \tag{20}$$

where λ_k for $k = 1,2,...,K$ represent the nonzero normalized eigenvalues (normalized by the maximum eigenvalue) of the

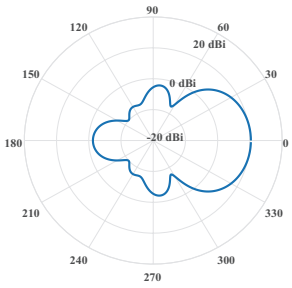

Fig. 3. Radiation pattern for the 5-element Yagi antenna. It has 10.4 dBi gain and an approximately 60 degree 3 dB beamwidth.

measurement matrix $\overline{\overline{H}}$ and P_k/N_0 is signal-to-noise ratio (SNR) [44]. Sensing capacity is also related to the concept of channel capacity in communications. K is known as the rank of $\overline{\overline{H}}$ and according to (20), sensing capacity increases with the number of non-zero eigenvalues of the measurement matrix. Higher sensing capacity is associated with characterizing greater information about the object gathered by the measurement system and also higher reconstruction quality. We use sensing capacity to characterize our pattern diversity configurations and determine which configurations would be best [43].

B. Pattern Diversity

To find sensing capacity for different antenna configurations we first need to obtain expressions for all the transmit $E^{\mathrm{i}}_{m,p}(\mathbf{r}_n)$ and receive $E^{\mathrm{i}}_{m',q}(\mathbf{r}_n)$ radiation fields so that the matrix $\overline{\overline{H}}$ can be evaluated using (16) and (18). To perform this straightforwardly we model the antenna patterns at all nodes by a single antenna pattern $F(\phi)$ and rotate it to obtain the P and Q different patterns.

We define $F(\phi)$ with its main beam pointing towards $\phi = 0^\circ$ (along the positive $x-$axis in Fig. 1) and write it as

$$F(\phi) = \sqrt{eD_0}E^n(\phi), \tag{21}$$

where $E^n(\phi) = \frac{|E(\phi)|}{|E(\phi)|_{\max}}$ denotes the normalized electric far-field antenna pattern, e is the radiation efficiency of the antenna. D_0 refers to the antenna's directivity and is defined as

$$D_0 = \frac{4\pi}{\int_\theta \left(E^n(\phi)\right)^2 \mathrm{d}\phi}. \tag{22}$$

To make the radiation pattern (21) realistic we utilize the pattern in the $x-y$ plane of a vertically polarized standard 5-element Yagi antenna with 10.4 dBi gain (two other patterns are also considered later). The pattern was obtained using full electromagnetic simulation using CST Studio Suite [46] and is shown in Fig. 3.

To form the P patterns at each transmission node we straightforwardly rotate the pattern by angle θ_p (to be determined later). The resulting antenna patterns are denoted as

$$F_p(\phi) = F(\phi - \theta_p). \tag{23}$$

To handle antennas on different parts of the boundary we additionally include another angle θ_m to rotate the main beam so that it is pointing inwards toward the DOI to arrive at

$$F_{m,p}(\phi) = F(\phi - \theta_m - \theta_p). \tag{24}$$

To be specific, $\theta_m = 0^\circ$ for the transceivers on the left vertical boundary, $\theta_m = 180^\circ$ for the transceivers on the right vertical boundary, $\theta_m = 270^\circ$ for the transceivers on the upper horizontal boundary and $\theta_m = 90^\circ$ for the transceivers on the bottom horizontal boundary. Nodes at the corners of the DOI are orientated along the diagonal of boundary so that $\theta_m = 45^\circ, 135^\circ, 225^\circ, 315^\circ$, for each corner respectively.

Using (24) the electric field radiated by transmitter m, pattern p is written as

$$E^{\mathrm{i}}_{m,p}(\mathbf{r}_n) = A_0 \cdot g(\mathbf{r}_m, \mathbf{r}_n) \cdot F(\phi_{m,n} - \theta_m - \theta_p), \tag{25}$$

where $\phi_{m,n}$ is the angle from the mth node to the nth pixel as shown in Fig. 1 and $A_0 = 1$ is the electric field amplitude.

Since the receivers and transmitters are the same we can use the same result (25) to also define the electric fields corresponding to the receiver patterns and this is achieved by interchanging m with m' and p with q.

C. Pattern Diversity Sensing Capacity

Using (25) we can find $\overline{\overline{H}}$ in (18) and therefore simulate sensing capacity through (20). The sensing capacity results of a 4, 5, 10 and 20-node system using the 5-element Yagi antenna pattern are shown in Fig. 4(a)-(d) respectively for when SNR$=$ 10 dB. In the simulations we use a single rotation parameter θ to specify the pattern rotation. Specifically for $P = 3$ there are three patterns with rotations $\theta_1 = -\theta$, $\theta_2 = 0$, $\theta_3 = \theta$. For $P = 2$ two pattern rotations are used and defined as $\theta_1 = -\theta$, $\theta_2 = 0$ and while for $P = 1$ there is no pattern diversity and $\theta_1 = 0$. The same rotation configurations are also applied to the Q receiver patterns. As θ increases from 0 the patterns become more independent and we observe sensing capacity increases until approximately $\theta = 55-65^\circ$ where the patterns are most different from each other. After that sensing capacity trails off slowly because the pattern has sidelobes and as long as the patterns remain reasonably uncorrelated the sensing capacity will remain good.

The number of unique independent links that can be obtained is given by $L = M(M-1)Q(P-Q/2)$ from (2). It should also be noted that since the transmit and receive patterns are the same and the different transmitters and receivers are co-located the sensing capacity results are identical for pattern configurations P, Q and Q, P and therefore results are only provided for unique P, Q pairs. In Fig. 4 we expect sensing capacity to increase with the total number of unique measurements given by $L = M(M-1)Q(P-Q/2)$ if all the patterns are completely independent. In the sensing capacity simulations L ranges from 6 ($M = 4, P = Q = 1$) to 1710 ($M = 20, P = Q = 3$) and we can therefore expect a 285 (1710/6) times increase in capacity from the lowest to highest link configurations. By checking Fig. 4(a)-(d), at $\theta = 60^\circ$ it can be seen however the ratio between the lowest sensing capacity configuration compared to the highest

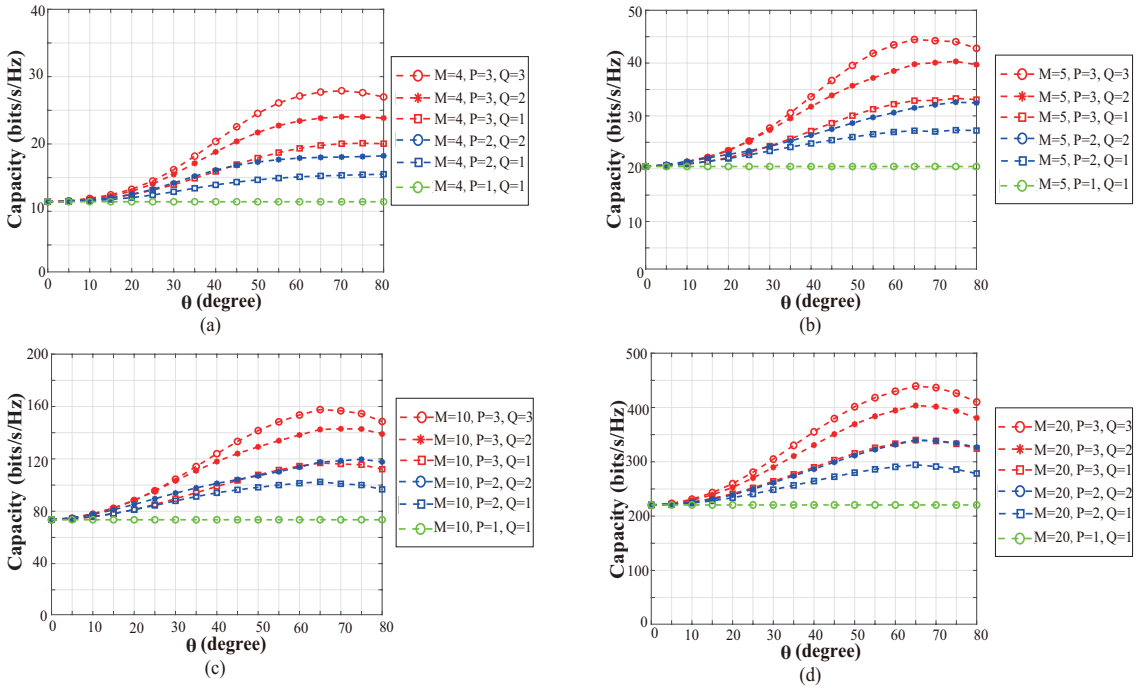

Fig. 4. Sensing capacity of $\overline{\overline{H}}$ with SNR=10 dB and where θ refers to the pattern rotation angle for different P and Q as defined in the associated text. The sub-figures refer to (a) 4-node imaging system, (b) 5-node imaging system, (c) 10-node imaging system and (d) 20-node imaging system.

is only around 40 when SNR= 10 dB. The relative increase in sensing capacity among different M, P, Q configurations becomes smaller as L increases. For example the increase in capacity from $M = 20, P = Q = 1$ to $M = 20, P = 3, Q = 3$ is only a factor of 3 (should be 9 by (2)) while that from $M = 20, P = Q = 1$ to $M = 20, P = 3, Q = 1$ is only 2 times (should be 5 by (2)). For $M = 4$ this relative increase is closer to that predicted by (2). This indicates that after a certain point the relative increase in diversity that can be created by the patterns starts to reduce. This is due to the large number of nodes and patterns covering the DOI and therefore the potential for further diversity decreases as the number of nodes increases.

The main objective of our sensing capacity investigation is to find a pattern configuration that can cut the number of nodes while maintaining a similar sensing capacity. From Fig. 4(c), we can see that the configuration of $M = 10$ with $P = 3$, $Q = 1$ for pattern rotation angles around $\theta = 60^\circ$ has sensing capacity nearly 2 times that for $M = 10$ with $P = Q = 1$ configuration. In addition in comparison with $M = 20$ with $P = Q = 1$ (Fig. 4(d)) it is providing similar sensing capacity. Using configurations $M = 10$ with $P = 3$, $Q = 1$ and $M = 20$ with $P = Q = 1$ we therefore expect reconstruction results to be similar to each other. In the next section we demonstrate the reconstructions achieved when using these configurations to confirm the conclusions from our sensing capacity simulations.

More generally we can use (2) as a rough rule of thumb for designing the imaging system patterns. For example to halve the number of nodes M required in a system with no pattern diversity ($L = M(M-1)/2$ links), then the system with pattern diversity ($L = M/2(M/2-1)Q(P-Q/2)$ links) should have the same number of links. That is $2Q(P-Q/2)$ should be greater than $4(M-1)/(M-2)$ or for large M, greater than 4. For small numbers of patterns this can be achieved when $P = Q = 2$ where $2Q(P-Q/2) = 4$ or when $P = 3$ with $Q = 1$ where $2Q(P-Q/2) = 5$ as we have found in the simulations provided above.

We have also investigated the effect of the shape of the antenna patterns on sensing capacity. In general, the key requirement for the patterns is that they provide acquisition of independent measurements so that inversion can proceed with less measurement nodes. That is any antenna pattern can be used as long as they can provide sufficient diversity within the DOI. To help support this proposition, sensing capacity results are also included for two additional radiation patterns as illustrated in Fig. 5. These radiation patterns are different from that in Fig. 3 and have narrower beamwidths with gain 15 dBi (Fig. 5(a)) and 17.3 dBi (Fig. 5(b)). The patterns are for sensing capacity analysis only and for reference were constructed by forming a 3- and 5-element linear array (with element separations of $\lambda/2$) in which the individual antenna element was the Yagi antenna with pattern in Fig. 3. Fig. 5(c)-(d) provide the corresponding sensing capacity for each of these patterns in a 4-node configuration. By studying Fig. 5, it can be observed that the sensing capacity with narrower beams can provide higher sensing capacity (at the maximum) as compared to the sensing capacity results using the radiation pattern of the Yagi antenna presented in Fig. 4(a). For example, at the maximum sensing capacity at around 60 degrees the sensing capacity is higher in Fig. 5 for the narrower patterns. This is due to the narrower main beam

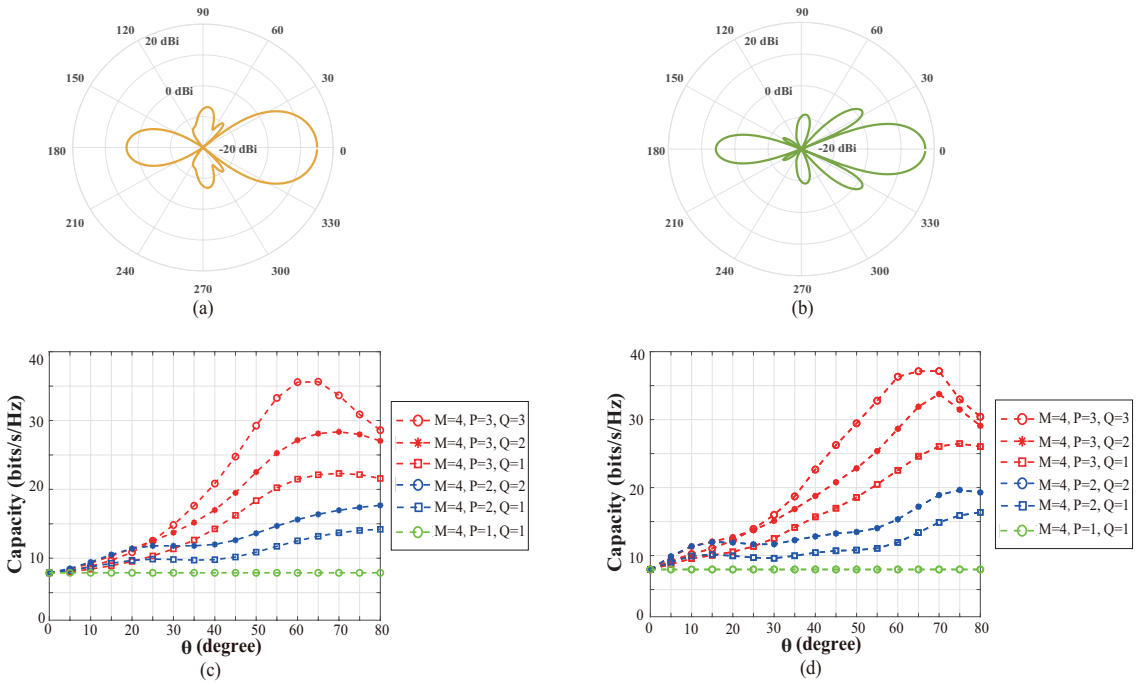

Fig. 5. The use of different patterns and corresponding sensing capacity of $\overline{\overline{H}}$ with SNR=10 dB of a 4-node system. Radiation patterns with a beamwidth of approximately (a) 40 degrees, 15 dBi gain and (b) 20 degrees and 17.3 dBi gain. The corresponding sensing capacity of the radiation patterns for (c) pattern in Fig. 5(a) and (d) pattern in Fig. 5(b). Here, θ refers to the pattern rotation angle for different P and Q as defined in the associated text.

being more focused. As the beam rotates, the narrow beam has relatively few overlapping sections and therefore provides more independence among the measurement results. This leads to an increase in sensing capacity. On the other hand, for the $P = Q = 1$ configuration (no beam steering or pattern diversity) the narrower beam has smaller sensing capacity. This is because the narrower beam without beam steering provides less coverage of the DOI. The narrower beams focus the radiation more and therefore parts of the DOI are not covered providing less sensing capacity.

The radiation patterns may also change shape and have different gain and shape with the rotation angle if electronic beam steering is utilized. To assess the effect of this we also consider patterns with different shape and gain in the measurement configuration. Specifically, considering a 4-node system again, the pattern for the $\theta_p = 0$ rotation is taken as the original 5-element Yagi antenna in Fig. 3 while for all other rotations the patterns are taken as that in Fig. 5(a). The corresponding results of the sensing capacity analysis are presented in Fig. 6. By studying Fig. 6, it can be observed that the sensing capacity of each configuration under the same P and Q as in Fig. 6 is slightly larger than the results obtained from rotating the single 5-element Yagi pattern shown in Fig. 4(a). This is again due to the narrower beam utilized for the rotated patterns in these simulations. The narrower beam has less overlap with the original Yagi pattern and therefore provides higher sensing capacity. This finding is consistent with the results presented in Fig. 5. It also shows that the shape of the rotated patterns does not need to be the same

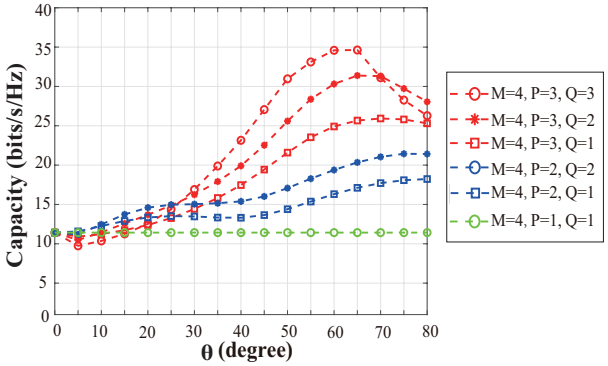

Fig. 6. Sensing capacity of $\overline{\overline{H}}$ when different patterns are used at different antenna rotations with SNR=10 dB of a 4-node system. The pattern for the rotation angles, $\theta_p = -\theta$ and $\theta_p = \theta$ is the radiation pattern shown in Fig. 5(a) and the pattern with rotation angle $\theta_p = 0$ remains the Yagi antenna pattern in Fig. 3. Again θ refers to the pattern rotation angle for different P and Q as defined in the associated text.

at different rotations. The patterns can be different as long as pattern diversity is achieved. Additionally note that since different radiation patterns are utilized at different rotation angles some links are also not reciprocal increasing diversity slightly too. For the $P = Q = 1$ note that sensing capacity is the same as the original results since there is no pattern diversity in this configuration.

V. Reconstruction Results

In this Section we detail simulated reconstruction results for the proposed antenna pattern diversity imaging system using full electromagnetic simulation software CST studio suite [46]. The operating frequency considered is $f = 2.4$ GHz and the corresponding wavelength is $\lambda = 125$ mm. The DOI size is 2×2 m^2 and the transceiver nodes are placed on its boundary as shown in Fig. 1. The boundary area is equivalent to $16\lambda \times 16\lambda$ and it is discretized into $N = 200 \times 200$ pixels with a $0.08\lambda \times 0.08\lambda$ pixel size so that there are in total $N = 40000$ unknowns. The rotation angle for the antenna patterns is taken as $\theta = 60^\circ$ which corresponds approximately to the maximum in sensing capacity found in the previous section. When $\theta = 0^\circ$ and $P = Q = 1$ there is no pattern diversity and we refer to this as conventional imaging [6]. The two sensing configurations we focus on are $M = 20, P = 3, Q = 1$ and $M = 10, P = 3, Q = 1$. We also use the conventional imaging configurations $M = 20, P = Q = 1$ and $M = 10, P = Q = 1$ as benchmarks.

Direct problem data is obtained by using full electromagnetic simulation software CST studio suite [46]. CST is widely accepted as an accurate 3D electromagnetic simulation tool and in our work the full antenna structure and 3D effects are incorporated. In particular in the CST simulations we take the cylinders as having a finite height of 2 m (± 1 m either side of the measurement x-y plane) and where all M nodes are configured with the 5-element Yagi with the pattern shown in Fig. 3. The simulations therefore provide realistic modeling of the 3D environment and antenna structure. The computations are performed on a CPU configured with a 2.4-GHz Intel Xeon Processor and 64-GB RAM. One simulation in which one node is configured as a transmit antenna with the remaining 19 nodes set as receivers takes approximately 2 hours. Therefore, if $M = 20$ nodes and $P = 3$ and $Q = 1$ patterns are considered, it takes about 120 hours to complete one simulation. Compared to direct problem simulations in 2D [3] the disadvantage of utilizing CST for the direct problem is the significantly increased simulation time (however the advantage is that the 3D CST results will be more realistic). For this reason we restrict the number of nodes to a maximum of $M = 20$ with $P = 3$ transmit patterns and $Q = 1$ receive patterns.

For better visualization, all the reconstructions are zoomed in on a 0.6 × 0.6 m^2 central area of the DOI to highlight the area around the scatterer (rather than showing reconstruction of the whole 2 × 2 m^2 area) and the pixel size is still 0.01×0.01 m^2 or equivalently $0.08\lambda \times 0.08\lambda$. The peak signal-to-noise ratio (PSNR) and structural similarity index (SSIM) results are provided for quantitative evaluation. Generally, the higher PSNR value or the closer SSIM is to unity, the better the reconstruction.

Three object configurations are considered in our reconstruction simulations. The first object configuration involves a single circular cylinder with 0.1 m radius (0.8λ) and homogeneous permittivity $\epsilon = 5 + 0.5j$ and $\epsilon = 15 + 1.5j$, respectively and the ground truth is provided in Fig. 7(a)-8(a). The second object configuration consists of two identical circular cylinders with radii 0.05 m (0.4λ) with homogeneous permittivity $\epsilon = 1.5 + 0.15j$ separated by 0.05 m (0.4λ) and $\epsilon = 5 + 0.5j$ separated by 0.2 m (1.6λ), respectively. The ground truth is provided in Fig. 9(a)-10(a) respectively. The third object configuration consists of two scatterers with different shapes and permittivities, including a rectangular object (0.1×0.2 m^2 ($0.8\lambda \times 1.6\lambda$)) with homogeneous permittivity $\epsilon = 2 + 0.2j$ and a circular object (radius 0.05 m (0.4λ)) with homogeneous permittivity $\epsilon = 5 + 0.5j$. The ground truth is provided in Fig. 11(a). Given the dimensions and the permittivity range of 1.5-15, the objects are beyond what BA and RA could accurately reconstruct [3]. Conventional BA and RA techniques would fail for these object permittivities and sizes considered and therefore xRA must be used and is a feature of this work.

Reconstruction results using pattern diversity with $M = 20, P = 3, Q = 1$ and $M = 10, P = 3, Q = 1$ are shown in Fig. 7(b)-11(b) and Fig. 7(c)-11(c) respectively. All reconstruction results are shown as the xRA contrast function $\mathrm{Im}\left(\boldsymbol{\chi}_{\mathrm{xRA}}\right) = \left(\frac{2}{\pi}\boldsymbol{\epsilon}_I\right)\sin^{-1}\left(1/\sqrt{\boldsymbol{\epsilon}_R}\right)$. For comparison and benchmarking, reconstructions with conventional imaging for $M = 20, P = 1, Q = 1$ and $M = 10, P = 1, Q = 1$ are provided in Fig. 7(d)-11(d) and Fig. 7(e)-11(e) respectively. In all figures the white dashed curve represents the boundary of the ground truth and the values of the color bar denote the reconstructed amplitude values of $\mathrm{Im}\left(\Delta\boldsymbol{\epsilon}_{\mathrm{xRA}}\right)$ and the PSNR and SSIM reconstruction results are listed in the figure captions.

Reconstruction results for the single circular cylinder with 0.1 m radius (0.8λ), $\epsilon = 5 + 0.5j$ ($\mathrm{Im}\left(\Delta\boldsymbol{\epsilon}_{\mathrm{xRA}}\right) = \left(\frac{2}{\pi}\boldsymbol{\epsilon}_I\right)\sin^{-1}\left(1/\sqrt{\boldsymbol{\epsilon}_R}\right) = 0.15$) are shown in Fig. 7. The reconstructions in Fig. 7(b)-(d) all provide good estimates of the object amplitude while that for $M = 10, P = 1, Q = 1$ in Fig. 7(e) is poor. The key result is in Fig. 7(c) confirms the sensing capacity results that a reduction to $M = 10$ nodes can be achieved without significant loss of reconstruction quality if pattern diversity is used (PSNR and SSIM is only slightly reduced). However if only 10 measurement nodes is used without pattern diversity reconstruction results are poor as shown in Fig. 7(e). Next, in Fig. 8, we increase the permittivity to $\epsilon = 15 + 1.5j$ and $\mathrm{Im}\left(\Delta\boldsymbol{\epsilon}_{\mathrm{xRA}}\right) = \left(\frac{2}{\pi}\boldsymbol{\epsilon}_I\right)\sin^{-1}\left(1/\sqrt{\boldsymbol{\epsilon}_R}\right) = 0.25$). Similar conclusions can be drawn to the previous results. That is the proposed antenna pattern diversity imaging system can achieve accurate reconstructions despite reducing the number of measurement nodes by half. Essentially the xRA validity range is not significantly affected by the use of pattern diversity and is similar to that of the original xRA results [3]. That is we can reduce the number of measurement nodes by approximately half without a reduction in validity range.

In order to investigate the resolution capabilities of the imaging system, simulation examples with two adjacent circular cylinders with low contrast ($\epsilon = 1.5 + 0.15j$ and $\mathrm{Im}\left(\Delta\boldsymbol{\epsilon}_{\mathrm{xRA}}\right) = \left(\frac{2}{\pi}\boldsymbol{\epsilon}_I\right)\sin^{-1}\left(1/\sqrt{\boldsymbol{\epsilon}_R}\right) = 0.09$) and higher contrast ($\epsilon = 5 + 0.5j$ and $\mathrm{Im}\left(\Delta\boldsymbol{\epsilon}_{\mathrm{xRA}}\right) = \left(\frac{2}{\pi}\boldsymbol{\epsilon}_I\right)\sin^{-1}\left(1/\sqrt{\boldsymbol{\epsilon}_R}\right) = 0.15$) are used to analyze the resolution capabilities. The radius of the circular scatterers are 0.05 m (0.4λ). We have found that for the lower contrast case we can distinguish the separation between the scatters until the

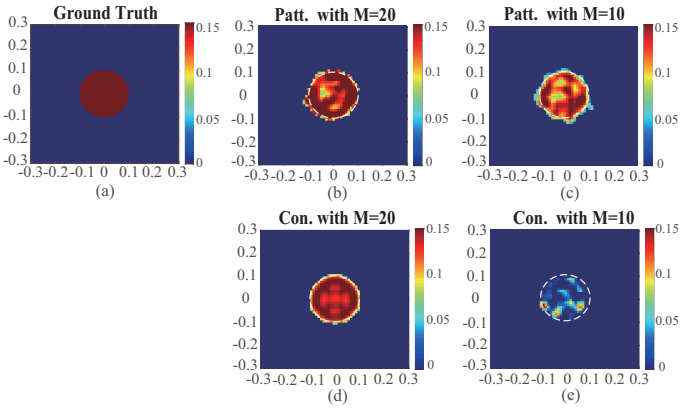

Fig. 7. Reconstruction results of a single circular cylinder with radius 0.1 m (0.8λ) and $\epsilon = 5+0.5j$ $\left(\mathrm{Im}\left(\Delta\boldsymbol{\epsilon}_{\mathrm{xRA}}\right) = \left(\frac{2}{\pi}\boldsymbol{\epsilon}_I\right)\sin^{-1}\left(1/\sqrt{\boldsymbol{\epsilon}_R}\right) = 0.15\right)$. (a) Ground truth scatter profile, (b)-(c) antenna-pattern diverse imaging system with 20 transceivers and 10 transceivers when $P = 3$ and $Q = 1$, (d)-(e) conventional imaging system with 20 transceivers and 10 transceivers and $P = 1$ and $Q = 1$. The respective PSNR and SSIM values of $\overline{\chi}_{\mathrm{xRA}}$ reconstructions are (b) (PSNR=24.93 dB, SSIM=0.99), (c) (PSNR=22.89 dB, SSIM=0.96), (d) (PSNR=24.52 dB, SSIM=0.99), and (e) (PSNR=12.89 dB, SSIM=0.87).

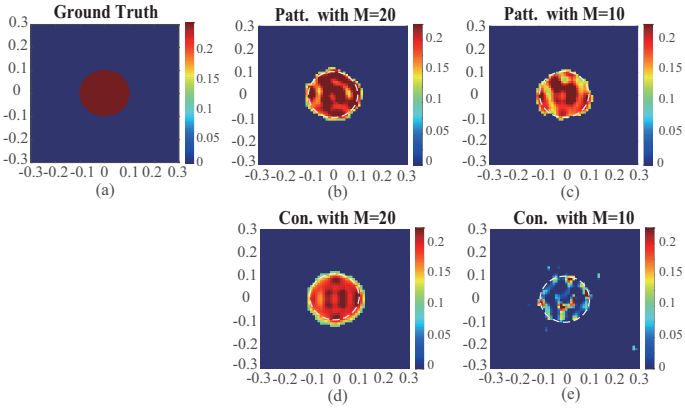

Fig. 8. Reconstruction results of a single circular cylinder with radius 0.1 m (0.8λ) and $\epsilon = 15 + 1.5j$ $\left(\mathrm{Im}\left(\Delta\boldsymbol{\epsilon}_{\mathrm{xRA}}\right) = \left(\frac{2}{\pi}\boldsymbol{\epsilon}_I\right)\sin^{-1}\left(1/\sqrt{\boldsymbol{\epsilon}_R}\right) = 0.25\right)$. (a) Ground truth scatter profile, (b)-(c) antenna-pattern diverse imaging system with 20 transceivers and 10 transceivers when $P = 3$ and $Q = 1$, (d)-(e) conventional imaging system with 20 transceivers and 10 transceivers and $P = 1$ and $Q = 1$. The respective PSNR and SSIM values of $\overline{\chi}_{\mathrm{xRA}}$ reconstructions are (b) (PSNR=21.73 dB, SSIM=0.92), (c) (PSNR=19.15 dB, SSIM=0.91), (d) (PSNR=21.64 dB, SSIM=0.91), and (e) (PSNR=15.31 dB, SSIM=0.86).

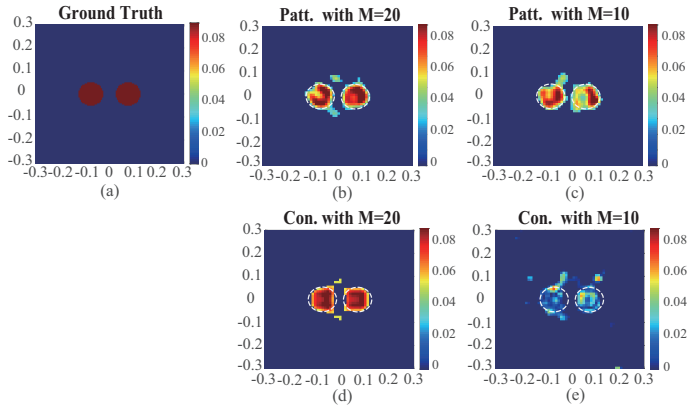

Fig. 9. Reconstruction results for two circular objects with radius 0.05 m (0.4λ), permittivity $\epsilon = 1.5 + 0.15j$ $\left(\mathrm{Im}\left(\Delta\boldsymbol{\epsilon}_{\mathrm{xRA}}\right) = \left(\frac{2}{\pi}\boldsymbol{\epsilon}_I\right)\sin^{-1}\left(1/\sqrt{\boldsymbol{\epsilon}_R}\right) = 0.09\right)$ and edge-to-edge separation 0.05 m (0.4λ). (a) Ground truth scatter profile, (b)-(c) antenna-pattern diverse imaging system with 20 transceivers and 10 transceivers when $P = 3$ and $Q = 1$, (d)-(e) conventional imaging system with 20 transceivers and 10 transceivers and $P = 1$ and $Q = 1$. The respective PSNR and SSIM values of $\overline{\chi}_{\mathrm{xRA}}$ reconstructions are (b) (PSNR=22.49 dB, SSIM=0.96), (c) (PSNR=20.28 dB, SSIM=0.95), (d) (PSNR=20.65 dB, SSIM=0.96), and (e) (PSNR=13.34 dB, SSIM=0.91).

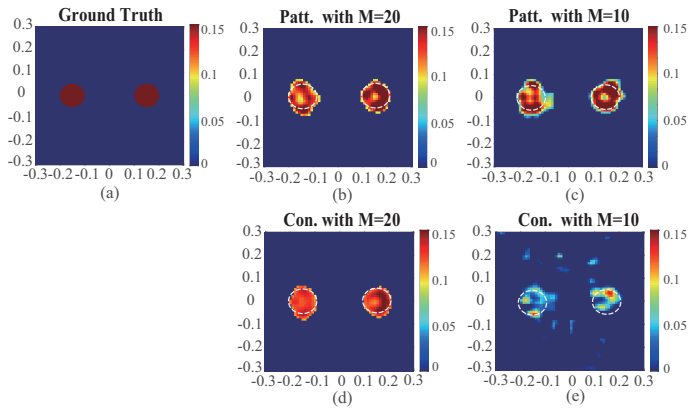

Fig. 10. Reconstruction results for two circular objects with radius 0.05 m (0.4λ), permittivity $\epsilon = 5 + 0.5j$ $\left(\mathrm{Im}\left(\Delta\boldsymbol{\epsilon}_{\mathrm{xRA}}\right) = \left(\frac{2}{\pi}\boldsymbol{\epsilon}_I\right)\sin^{-1}\left(1/\sqrt{\boldsymbol{\epsilon}_R}\right) = 0.15\right)$ and edge-to-edge separation 0.2 m (1.6λ). (a) Ground truth scatter profile, (b)-(c) antenna-pattern diverse imaging system with 20 transceivers and 10 transceivers when $P = 3$ and $Q = 1$, (d)-(e) conventional imaging system with 20 transceivers and 10 transceivers and $P = 1$ and $Q = 1$. The respective PSNR and SSIM values of $\overline{\chi}_{\mathrm{xRA}}$ reconstructions are (b) (PSNR=21.12 dB, SSIM=0.92), (c) (PSNR=18.45 dB, SSIM=0.89), (d) (PSNR=19.62 dB, SSIM=0.91), and (e) (PSNR=14.48 dB, SSIM=0.87).

edge-to-edge separation is around 0.05 m (0.4λ). However, the system cannot distinguish the separation for the higher contrast object until their separation is 0.2 m (1.6λ). The results for these separations and contrast are provided in Fig. 9-10. They indicate that the resolution of the imaging system is affected by the dielectric properties of the scatterers. This is most likely due to the stronger scattering by the high contrast object making the xRA formulation less accurate. However, it can be seen in Fig. 9-10 that the proposed antenna pattern diversity imaging system still performs well in comparison to the conventional approach and performs similarly to the conventional single node configuration.

We have also extended our investigation to encompass scatterers consisting of rectangular (0.1×0.2 m^2 ($0.8\lambda\times1.6\lambda$)) and circular (radius 0.05 m (0.4λ)) cylinders with permittivity values ranging from $\epsilon = 2+0.2j$ to $\epsilon = 5+0.5j$ and edge-to-edge separation 0.2 m (1.6 λ). The reconstruction results are provided in Fig. 11. Both objects can be well reconstructed along with their permittivity values with using only half of the measurement nodes.

The technique can also be extended to 3D. The most straightforward method to perform this is to acquire measurements across multiple cross-sections by scanning the measurement nodes along the z-axis. The cross-sections at each z-axis scan position can be reconstructed and put together

TABLE I
RELATIVE PERFORMANCE OF DIFFERENT WORK.

Reported work	Antenna	Diversity Scheme	Bandwidth	f_0 (GHz)	Imaging Dimension	Imaging Region $(Width \times Length)$	Number of Antennas	Recons. Approach	Maximum Recons. Object Permittivity
In [3]	Yagi antenna	N/A	0 Hz	2.4	2D	24 λ × 24 λ	20-40	xRA	Dielectric, $\epsilon \approx 15$
In [47]	Metamaterial frequency diverse antennas	Frequency diversity	9 GHz	21.75	2D	142.9 λ × 214.3 λ	6	BA	Dielectric, $\epsilon \approx 2.25$
In [48]	Frequency-diverse Mill-Cross cavity aperture antennas	Frequency diversity	8.5 GHz	22.5	3D	76.9 λ × 76.9 λ	12	BA	Metal
In [49]	Programmable metasurface phase shifter antenna	Pattern diversity	0 Hz	5.65	2D	3.8 λ × 3.8 λ	64	BA	Metal
In [50]	Two-layer programmable metasurface antenna	Pattern diversity	0 Hz	9.2	2D	15.6 λ × 15.6 λ	25	N/A	Metal
Our Work	Yagi antenna (arbitrary directional or reconfigurable antennas)	Pattern diversity	0 Hz	2.4	2D (&3D)	16 λ × 16 λ	10	xRA	Dielectric, $\epsilon \approx 15$

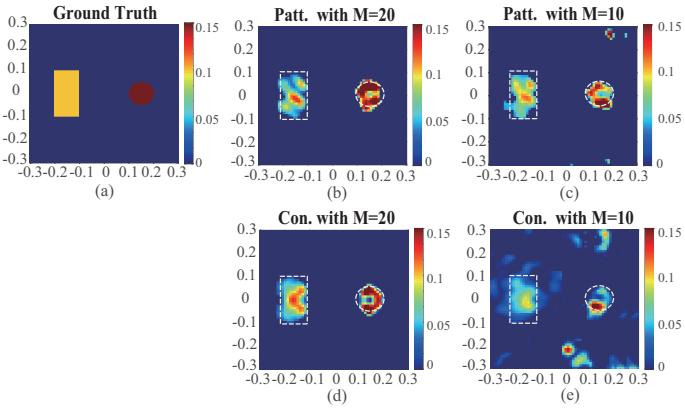

Fig. 11. Reconstruction results for rectangular (0.1×0.2 m^2 ($0.8\lambda \times 1.6\lambda$)) and circular (radius 0.05 m (0.4λ)) cylinder objects that have permittivity's $\epsilon = 2 + 0.2j$ $\left(\text{Im}\left(\Delta\boldsymbol{\epsilon}_{\text{xRA}}\right) = \left(\frac{2}{\pi}\boldsymbol{\epsilon}_I\right)\sin^{-1}\left(1/\sqrt{\boldsymbol{\epsilon}_R}\right) = 0.1\right)$ and $\epsilon = 5 + 0.5j$ $\left(\text{Im}\left(\Delta\boldsymbol{\epsilon}_{\text{xRA}}\right) = \left(\frac{2}{\pi}\boldsymbol{\epsilon}_I\right)\sin^{-1}\left(1/\sqrt{\boldsymbol{\epsilon}_R}\right) = 0.15\right)$ respectively. The edge-to-edge separation is 0.2 m (1.6λ). (a) Ground truth scatter profile, (b)-(c) antenna-pattern diverse imaging system with 20 transceivers and 10 transceivers when $P = 3$ and $Q = 1$, (d)-(e) conventional imaging system with 20 transceivers and 10 transceivers and $P = 1$ and $Q = 1$. The respective PSNR and SSIM values of $\overline{\chi}_{\text{xRA}}$ reconstructions are (b) (PSNR=24.72 dB, SSIM=0.92), (c) (PSNR=20.39 dB, SSIM=0.89), (d) (PSNR=21.75 dB, SSIM=0.91), and (e) (PSNR=15.95 dB, SSIM=0.77).

to obtain a full 3D reconstruction by using half the number of sensing nodes if our pattern diversity system is utilized. Preliminary simulation results we have obtained show that for such a 3D imaging approach, for a circular cylinder with radius 0.05 m, height 0.04 m and permittivity $\epsilon = 3 + 0.3j$ and z-axis scanning intervals of 0.02 m, has provided promising results. In summary, our reconstruction results support and verify the findings from sensing capacity simulations. Our proposed imaging system with antenna pattern diversity can provide similar reconstruction performance compared to that of a conventional imaging system but with half the number of measurement nodes.

VI. DISCUSSION

It is shown that the proposed pattern diversity imaging system provides good reconstruction results with half the number of measurement nodes required compared to the conventional imaging system without pattern diversity. This is because the pattern diversity imaging system can provide more independent measurements by incorporating pattern diversity without adding more nodes.

Comparisons with other relevant imaging systems are shown in Table I, where f_0 is central frequency. The comparisons include systems featuring conventional, programmable metasurface and frequency-diverse antenna approaches. Metasurface and frequency-diverse antennas have been previously proposed to also circumvent the large number of transceivers required and reduce the system cost of the conventional imaging configuration. In Table I the column with 'Bandwidth' where some entries are listed as 0 Hz refers to single carrier or single tone systems. The column with 'Imaging Region' refers to the size of the DOI where λ refers to the corresponding wavelength in the respective system. The column with 'Number of Antennas' provides the number of the antennas used. The column with 'Maximum Recons. Object Permittivity' provides the maximum accurately reconstructed permittivity example in their work.

The proposed frequency-diverse imaging systems in [47], [48] require wideband operation due to their highly dispersive structures providing frequency diversity and this leads to higher imaging performance. However, due to the fundamental tradeoff between high scanning rate and low efficiency in dispersive structures, i.e., leaky-wave antennas (LWAs), the antennas used in this system inevitably suffer from low radiation efficiency [22], [23], [24], [25]. In addition, for imaging systems based on programmable metasurface components, varactor diodes are integrated into the unit cells to achieve continuous control and full coverage of the transmission phase in designing the programmable metasurface [49], [50]. In our approach a single frequency is only required and straightforward pattern diversity is utilized to overcome hardware complexity issues. Although we utilize the Yagi antenna as an example to demonstrate the antenna pattern diversity scheme, it can be conveniently implemented using reconfigurable antennas [27]. Overall, the comparisons show that the proposed antenna pat-

tern diversity imaging system reduces the number of required measurement nodes without intricate antenna structures while providing high reconstruction accuracy for 2D and 3D imaging scenarios, and utilizes a single frequency.

VII. Conclusions

In this paper we have proposed an antenna pattern diversity imaging system utilizing xRA that can reduce the required number of measurement nodes by up to half compared to conventional RF and microwave imaging systems. We have analyzed the proposed imaging system using the concept of sensing capacity, to conveniently find suitable antenna pattern diversity configurations for halving the number of sensing nodes while maintaining reconstruction quality. Results demonstrating the reconstruction of objects consisting of single and multiple scatterers with different shapes and different permittivity have been provided. These results demonstrate that the proposed antenna pattern diversity imaging system can provide accurate image reconstruction even though the number of measurement nodes has been reduced by half. To further validate this technique, experimental verification should be considered in the future.

References

[1] A. S. Beaverstone, D. S. Shumakov, and N. K. Nikolova, "Frequency-domain integral equations of scattering for complex scalar responses," *IEEE Trans. Microwave Theory Tech.*, vol. 65, no. 4, pp. 1120–1132, 2017.

[2] D. S. Shumakov and N. K. Nikolova, "Fast quantitative microwave imaging with scattered-power maps," *IEEE Trans. Microwave Theory Tech.*, vol. 66, no. 1, pp. 439–449, 2018.

[3] A. Dubey, S. Deshmukh, L. Pan, X. Chen, and R. Murch, "A phaseless extended Rytov approximation for strongly scattering low-loss media and its application to indoor imaging," *IEEE Trans. Geosci. Remote Sens.*, vol. 60, pp. 1–17, 2022.

[4] S. Depatla, L. Buckland, and Y. Mostofi, "X-ray vision with only WiFi power measurements using Rytov wave models," *IEEE Trans. Veh. Technol.*, vol. 64, no. 4, pp. 1376–1387, 2015.

[5] S. Deshmukh, A. Dubey, D. Ma, Q. Chen, and R. Murch, "Physics assisted deep learning for indoor imaging using phaseless Wi-Fi measurements," *IEEE Trans. Antennas Propag.*, vol. 70, no. 10, pp. 9716–9731, 2022.

[6] A. Dubey, P. Sood, J. Santos, D. Ma, C.-Y. Chiu, and R. Murch, "An enhanced approach to imaging the indoor environment using WiFi RSSI measurements," *IEEE Trans. Veh. Technol.*, vol. 70, no. 9, pp. 8415–8430, 2021.

[7] R. Zoughi, *Microwave non-destructive testing and evaluation principles*. Springer Science & Business Media, 2000, vol. 4.

[8] A. Zamani, A. M. Abbosh, and A. T. Mobashsher, "Fast frequency-based multistatic microwave imaging algorithm with application to brain injury detection," *IEEE Trans. Microw. Theory Tech.*, vol. 64, no. 2, pp. 653–662, 2016.

[9] R. Chandra, H. Zhou, I. Balasingham, and R. M. Narayanan, "On the opportunities and challenges in microwave medical sensing and imaging," *IEEE Trans. Biomed. Eng.*, vol. 62, no. 7, pp. 1667–1682, 2015.

[10] R. Scapaticci, P. Kosmas, and L. Crocco, "Wavelet-based regularization for robust microwave imaging in medical applications," *IEEE Trans. Biomed. Eng.*, vol. 62, no. 4, pp. 1195–1202, 2015.

[11] S. Di Meo, P. F. Espin-Lopez, A. Martellosio, M. Pasian, G. Matrone, M. Bozzi, G. Magenes, A. Mazzanti, L. Perregrini, F. Svelto *et al.*, "On the feasibility of breast cancer imaging systems at millimeter-waves frequencies," *IEEE Trans. Microwave Theory Tech.*, vol. 65, no. 5, pp. 1795–1806, 2017.

[12] Z. Wei, D. Liu, and X. Chen, "Dominant-current deep learning scheme for electrical impedance tomography," *IEEE Trans. Biomed. Eng.*, vol. 66, no. 9, pp. 2546–2555, 2019.

[13] Z. Ma, K. Xu, R. Song, C.-F. Wang, and X. Chen, "Learning-based fast electromagnetic scattering solver through generative adversarial network," *IEEE Trans. Antennas Propag.*, vol. 69, no. 4, pp. 2194–2208, 2021.

[14] S. Deshmukh, A. Dubey, and R. Murch, "Unrolled optimization with deep learning-based priors for phaseless inverse scattering problems," *IEEE Trans. Geosci. Remote Sens.*, vol. 60, pp. 1–14, 2022.

[15] D. Tajik, D. S. Shumakov, and N. K. Nikolova, "An experimental comparison between the Born and Rytov approximations in microwave tissue imaging," in *2017 IEEE MTT-S International Microwave Symposium (IMS)*, 2017, pp. 1391–1393.

[16] J. Wilson and N. Patwari, "Radio tomographic imaging with wireless networks," *IEEE Trans. Mob. Comput.*, vol. 9, no. 5, pp. 621–632, 2010.

[17] Q. Wang, H. Yiğitler, R. Jäntti, and X. Huang, "Localizing multiple objects using radio tomographic imaging technology," *IEEE Trans. Veh. Technol.*, vol. 65, no. 5, pp. 3641–3656, 2015.

[18] Y. Zhao, N. Patwari, J. M. Phillips, and S. Venkatasubramanian, "Radio tomographic imaging and tracking of stationary and moving people via kernel distance," in *2013 ACM/IEEE International Conference on Information Processing in Sensor Networks (IPSN)*. IEEE, 2013, pp. 229–240.

[19] B. Wei, A. Varshney, N. Patwari, W. Hu, T. Voigt, and C. T. Chou, "dRTI: Directional radio tomographic imaging," in *Proceedings of the 14th International Conference on Information Processing in Sensor Networks*, 2015, pp. 166–177.

[20] O. Kaltiokallio, R. Jäntti, and N. Patwari, "ARTI: An adaptive radio tomographic imaging system," *IEEE Trans. Veh. Technol.*, vol. 66, no. 8, pp. 7302–7316, 2017.

[21] O. Yurduseven, V. R. Gowda, J. N. Gollub, and D. R. Smith, "Multistatic microwave imaging with arrays of planar cavities," *IET Microwaves, Antennas & Propagation*, vol. 10, no. 11, pp. 1174–1181, 2016.

[22] G. Zhang, Q. Zhang, S. Ge, Y. Chen, and R. D. Murch, "High scanning-rate leaky-wave antenna using complementary microstrip-slot stubs," *IEEE Trans. Antennas Propag.*, vol. 67, no. 5, pp. 2913–2922, 2019.

[23] D. Ma, J. Zhong, S. Shen, A. Dubey, C. Zhang, Q. Zhang, and R. Murch, "Single-shot frequency-diverse near-field imaging using high-scanning-rate leaky-wave antenna," *IEEE Trans. Microwave Theory Tech.*, vol. 69, no. 7, pp. 3399–3412, 2021.

[24] G. Zhang, Q. Zhang, Y. Chen, and R. D. Murch, "High-scanning-rate and wide-angle leaky-wave antennas based on glide-symmetry goubau line," *IEEE Trans. Antennas Propag.*, vol. 68, no. 4, pp. 2531–2540, 2020.

[25] D.-F. Guan, Q. Zhang, P. You, Z.-B. Yang, Y. Zhou, and S.-W. Yong, "Scanning rate enhancement of leaky-wave antennas using slow-wave substrate integrated waveguide structure," *IEEE Trans. Antennas Propag.*, vol. 66, no. 7, pp. 3747–3751, 2018.

[26] R. Vaughan, "Switched parasitic elements for antenna diversity," *IEEE Trans. Antennas Propag.*, vol. 47, no. 2, pp. 399–405, 1999.

[27] P. Lotfi, S. Soltani, and R. D. Murch, "Printed endfire beam-steerable pixel antenna," *IEEE Trans. Antennas Propag.*, vol. 65, no. 8, pp. 3913–3923, 2017.

[28] M. A. Towfiq, I. Bahceci, S. Blanch, J. Romeu, L. Jofre, and B. A. Cetiner, "A reconfigurable antenna with beam steering and beamwidth variability for wireless communications," *IEEE Trans. Antennas Propag.*, vol. 66, no. 10, pp. 5052–5063, 2018.

[29] Y. Zhang, Z. Han, S. Tang, S. Shen, C.-Y. Chiu, and R. Murch, "A highly pattern-reconfigurable planar antenna with 360 degree single- and multi-beam steering," *IEEE Trans. Antennas Propag.*, pp. 1–1, 2022.

[30] Z. Wei and X. Chen, "Physics-inspired convolutional neural network for solving full-wave inverse scattering problems," *IEEE Trans. Antennas Propag.*, vol. 67, no. 9, pp. 6138–6148, 2019.

[31] X. Chen, *Computational methods for electromagnetic inverse scattering*. Wiley Online Library, 2018.

[32] L. Guo, N. Nguyen-Trong, A. Ai-Saffar, A. Stancombe, K. Bialkowski, and A. Abbosh, "Calibrated frequency-division distorted Born iterative tomography for real-life head imaging," *IEEE Trans. Med. Imaging*, vol. 41, no. 5, pp. 1087–1103, 2021.

[33] L. Guo, M. Khosravi-Farsani, A. Stancombe, K. Bialkowski, and A. Abbosh, "Adaptive clustering distorted Born iterative method for microwave brain tomography with stroke detection and classification," *IEEE Trans. Biomed. Eng.*, vol. 69, no. 4, pp. 1512–1523, 2021.

[34] X. Ye and X. Chen, "Subspace-based distorted Born iterative method for solving inverse scattering problems," *IEEE Trans. Antennas Propag.*, vol. 65, no. 12, pp. 7224–7232, 2017.

[35] R. K. Amineh, M. Ravan, and R. Sharma, "Nondestructive testing of nonmetallic pipes using wideband microwave measurements," *IEEE Trans. Microwave Theory Tech.*, vol. 68, no. 5, pp. 1763–1772, 2020.

[36] A. Dubey, X. Chen, and R. Murch, "A new correction to the Rytov approximation for strongly scattering lossy media," *IEEE Trans. Antennas Propag.*, vol. 70, no. 11, pp. 10 851–10 864, 2022.

[37] D. Ma, Y. Zhang, A. Dubey, S. Deshmukh, S. Shen, Q. Zhang, and R. Murch, "Millimeter-wave 3-D imaging using leaky-wave antennas and an extended Rytov approximation in a frequency-diverse MIMO system," *IEEE Trans. Microwave Theory Tech.*, pp. 1–17, 2022.

[38] L. Zhang, K. Xu, R. Song, X. Ye, G. Wang, and X. Chen, "Learning-based quantitative microwave imaging with a hybrid input scheme," *IEEE Sensors Journal*, vol. 20, no. 24, pp. 15 007–15 013, 2020.

[39] N. K. Nikolova, *Introduction to microwave imaging*. Cambridge University Press, 2017.

[40] W. Wang, L. Jing, Z. Li, and R. D. Murch, "Utilizing the Born and Rytov inverse scattering approximations for detecting soft faults in lossless transmission lines," *IEEE Trans. Antennas Propag.*, vol. 65, no. 12, pp. 7233–7243, 2017.

[41] A. C. Kak and M. Slaney, *Principles of computerized tomographic imaging*. SIAM, 2001.

[42] J. M. Bioucas-Dias and M. A. Figueiredo, "A new TwIST: Two-step iterative shrinkage/thresholding algorithms for image restoration," *IEEE Trans. Image Process.*, vol. 16, no. 12, pp. 2992–3004, 2007.

[43] J. A. M. Lorenzo, J. H. Juesas, and W. Blackwell, "A single-transceiver compressive reflector antenna for high-sensing-capacity imaging," *IEEE Antennas Wirel. Propag. Lett.*, vol. 15, pp. 968–971, 2015.

[44] P. del Hougne, "Robust position sensing with wave fingerprints in dynamic complex propagation environments," *Physical Review Research*, vol. 2, no. 4, p. 043224, 2020.

[45] X. Chen, "Application of signal-subspace and optimization methods in reconstructing extended scatterers," *JOSA A*, vol. 26, no. 4, pp. 1022–1026, 2009.

[46] *CST Microwave Studio 2021*. Accessed: Jan. 1, 2022. [Online]. Available: https://www.cst.com.

[47] J. Hunt, T. Driscoll, A. Mrozack, G. Lipworth, M. Reynolds, D. Brady, and D. R. Smith, "Metamaterial apertures for computational imaging," *Science*, vol. 339, no. 6117, pp. 310–313, 2013.

[48] O. Yurduseven, J. N. Gollub, D. L. Marks, and D. R. Smith, "Frequency-diverse microwave imaging using planar mills-cross cavity apertures," *Opt. Express*, vol. 24, no. 8, pp. 8907–8925, Apr 2016.

[49] H. Li, Y. B. Li, G. Chen, S. Y. Dong, J. L. Shen, C. Y. Gong, S. Y. Wang, H. P. Wang, and T. J. Cui, "High-resolution near-field imaging and far-field sensing using a transmissive programmable metasurface," *Adv. Mater. Technol.*, p. 2101067, 2021.

[50] Y. B. Li, L. L. Li, B. B. Xu, W. Wu, R. Y. Wu, X. Wan, Q. Cheng, and T. J. Cui, "Transmission-type 2-bit programmable metasurface for single-sensor and single-frequency microwave imaging," *Sci. Rep.*, vol. 6, no. 1, pp. 1–8, 2016.

Dingfei MA (Graduate Student Member, IEEE) received the B.E. degree from the Harbin Institute of Technology, Harbin, China, in 2017, and the joint M.Sc. degree from the Harbin Institute of Technology, Harbin, China, and the Southern University of Science and Technology (SUSTech), Shenzhen, China, in 2019, and Ph.D. degrees in electronic and computer engineering from the Hong Kong University of Science and Technology (HKUST), Hong Kong, in 2023, respectively. She is currently a Post-Doctoral Researcher with HKUST.

Her research include leaky-wave antenna design, inverse scattering problems, machine learning, integrated sensing & communication system and internet of things.

Amartansh Dubey (Member, IEEE) received the Ph.D. in Electronic and Computer Engineering from the Hong Kong University of Science and Technology (HKUST) in 2022, before which he obtained his MPhil from HKUST in 2018 and bachelor's degree from Visvesvaraya National Institute of Technology (VNIT), India in 2016. He is currently a Research Assistant Professor (RAP) at HKUST.

His research interests include Inverse Scattering, Indoor RF Imaging & Sensing (using ambient Wi-Fi), Physics-informed Machine Learning, Joint communication & Imaging, Applied Random Matrix Theory, and Radio & Microwave Imaging. He has won more than 10 prestigious fellowships and awards at national, international & university levels which includes the prestigious IEEE Antenna & Propagation fellowship (IEEE APSF award 2022) for his contributions to indoor imaging and sensing using inverse scattering.

Zihao Xu (Graduate Student Member, IEEE) received the B.E. degree from the Southern University of Science and Technology, Shenzhen, in 2022. He is currently pursuing the Ph.D. degree at the Hong Kong University of Science and Technology, Hong Kong. His research interests include leaky-wave antennas and microwave imaging system design.

Shanpu Shen (Senior Member, IEEE) received the bachelor's degree in communication engineering from the Nanjing University of Science and Technology, Nanjing, China, in 2013, and the Ph.D. degree in electronic and computer engineering from The Hong Kong University of Science and Technology (HKUST), Hong Kong, in 2017.

He was a Visiting Ph.D. Student with the Microsystems Technology Laboratories, Massachusetts Institute of Technology, Cambridge, MA, USA, in 2016. He was a Post-Doctoral Fellow with HKUST from 2017 to 2018 and a Post-Doctoral Research Associate with the Communications and Signal Processing Group, Imperial College London, London, U.K., from 2018 to 2020. He was a Research Assistant Professor with the Department of Electronic and Computer Engineering, HKUST, from 2020 to 2023. He is currently a Lecturer (Assistant Professor) with the Department of Electrical Engineering and Electronics, University of Liverpool, U.K.

His current research interests include RF energy harvesting, wireless power transfer, reconfigurable intelligent surface, Internet-of-Things, MIMO systems, and antenna design and optimization.

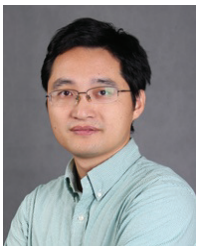

Qingfeng Zhang (Senior Member, IEEE) received the B.E. degree in electrical engineering from the University of Science and Technology of China (USTC), Hefei, China, in 2007, and the Ph.D. degree in electrical engineering from Nanyang Technological University, Singapore, in 2011. From June 2011 to December 2013, he was a Post-Doctoral Fellow with the Poly-Grames Research Center, Ecole Polytechnique de Montreal, Montreal, QC, Canada. Since December 2013, he has been with Southern University of Science and Technology (SUSTech), Shenzhen, China, where he is currently an Professor. His research interests are largely in emerging novel electromagnetics technologies in which he has a special interest in dispersion engineering at microwave and millimeter-wave frequencies.

Dr. Zhang has served as a TPC member for various international conferences and on the review board of numerous journals in electromagnetics. He is also a fellow of the Institution of Engineering and Technology (IET). He received the URSI Young Scientist Award and the ACES Young Scientist Award in 2018. He is also the Vice-Chair of the IEEE Antennas and Propagation Society Shenzhen Chapter. He was the Publication Chair of the 2016 IEEE International Conference on Communication Systems (ICCS), the Local Organization Committee Co-Chair of 2017 IEEE Electrical Design of Advanced Packaging and Systems (EDAPS) Symposium, the TPC Co-Chair of Track 9 (Passive ICs and Active Antennas) in 2018 IEEE International Conference on Integrated Circuits, Technologies and Applications (ICTA), and the Track Chair of 2019 ComComAp. He has served as a Lead Guest Editor for the International Journal of Antennas and Propagation from 2014 to 2015. He has been serving as an Associate Editor for IEEE ACCESS since 2017.

Ross Murch (S'84-M'90-SM'98-F'09) received the bachelor's and Ph.D. degrees in electrical and electronic engineering from the University of Canterbury, Christchurch, New Zealand, in 1987 and 1990, respectively

He is currently a Chair Professor in the Department of Electronic and Computer Engineering and a Senior Fellow at the Institute of Advanced Study both at the Hong Kong University of Science and Technology (HKUST). He is known for his research on multiple antenna technology including multiuser-MIMO, compact multiport antennas and multiport energy harvesting. His current research focus is creating new RF wave technology for making a better world and this includes RF imaging, ambient RF systems, energy harvesting, electromagnetic information theory, 6G, IoT, multiport antenna systems and reconfigurable intelligent surfaces. His unique expertise lies in his combination of knowledge from both wireless communication systems and electromagnetics and he publishes in both areas. In total his research contributions include over 200 journal publications and more than 20 patents while successfully supervising more than 50 research students. Prof. Murch also has a strong interest in education, enjoys teaching and has won five teaching awards.

Prof. Murch was Department Head at HKUST from 2009-2015, is an IEEE, IET, HKIE, and FHKEng Fellow. He has been a David Bensted Fellow, Simon Fraser University, Canada, an HKTIIT fellow at Southampton University, U.K and has spent sabbaticals at MIT, USA; AT&T, USA; Allgon Mobile Communications, Sweden; Imperial College London, He has served IEEE in various positions including IEEE area editor, technical program chair, distinguished lecturer and Fellow evaluation committee.

Prof. Murch joined HKUST in 1992 as an Assistant Professor and has remained at HKUST in Hong Kong since then, where he is now a Chair Professor. From 1990-1992 he was a Post-Doctoral Fellow at the Department of Mathematics and Computer Science, University of Dundee, UK.